Electronic Supplementary Material (ESI) for Nanoscale.

Enhanced room-temperature terahertz detection and imaging derived from anti-reflection 2D perovskite layer on $MAPbI_3$ single crystals

*Junyu Li[1], Yousheng Zou[1], Dawei Hu[1], Yu Gu[1], Zeyao Han[1], Jiaxin Liu[1], Xiaobao Xu[1]**

MIIT Key Laboratory of Advanced Display Materials and Devices, College of Materials Science and Engineering, Nanjing University of Science and Technology Nanjing 210094, China

E-mail: xiaobaoxu@njust.edu.cn

The reference of Figure 1c. Conventional semiconductors: Si,[1-4] GaAs,[5-8] CZTS(Se)[9-11]; thermoelectric materials: SnTe,[12-16] GeTe,[17-19] PbTe,[20-22] BiCuSeO,[23-25] Mg_3Sb_2,[26-30] Bi_2Te_3,[31-33] SnSe[34-36]; perovskite[37-39].

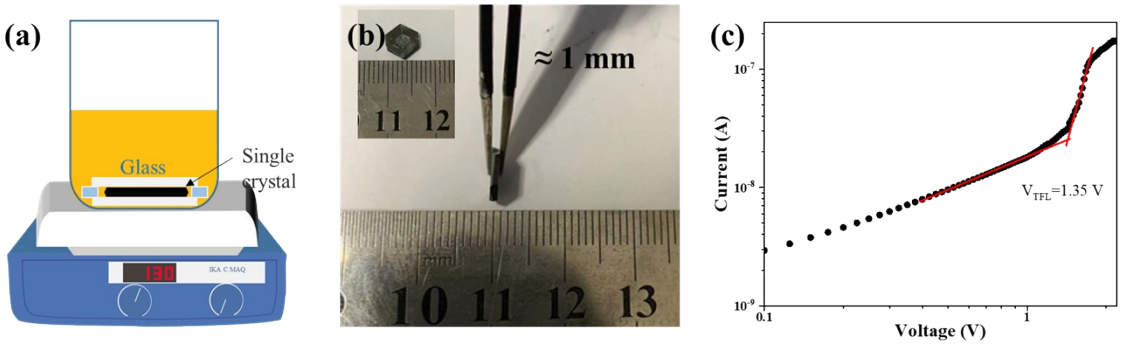

Figure S1. a) Schematic illustration of space-limited SCs preparation. b) Side and top view photographs of the space-limited $MAPbI_3$ SC. c) Dark current-voltage curve of $MAPbI_3$ SC for SCLC.

For SCLC measurement, a quadratic relation between dark current and voltage is expected and the current density and voltage followed the Equation (1):

$$J_D = \frac{9\varepsilon\varepsilon_0\mu V^2}{8L^3} \quad (1)$$

Meanwhile, at the turning point, n_{trap} can be estimated by Equation (2):

$$n_{trap} = \frac{2\varepsilon\varepsilon_0 V_{TFL}}{qL^2} \quad (2)$$

where ε represents the relative dielectric constant, ε_0 represents the vacuum permittivity and L represents for the thickness of SCs. The relative dielectric constant of $MAPbI_3$ is about 18.[40, 41] And the electrodes area of SC is about 3 mm×3 mm. Thus, the mobility and trap density of $MAPbI_3$ SC are μ=96.81 $cm^2\ V^{-1}\ s^{-1}$ and n_{trap}=2.686×10^9 cm^{-3}.

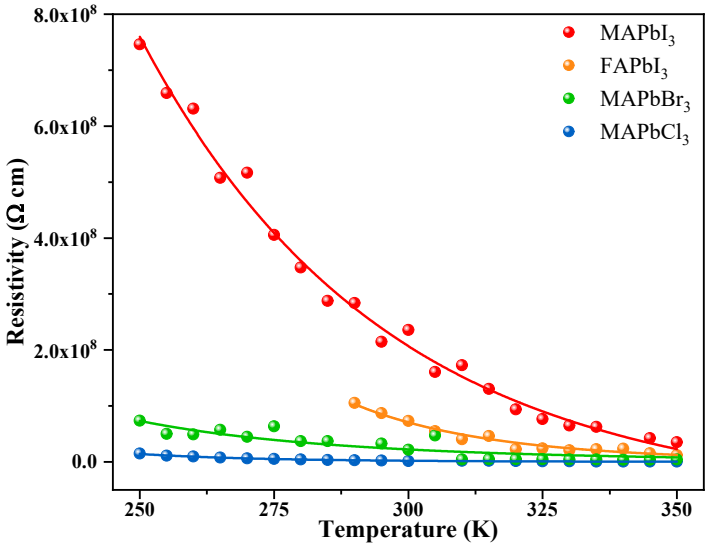

Figure S2. Resistivity-temperature curves of different SCs.

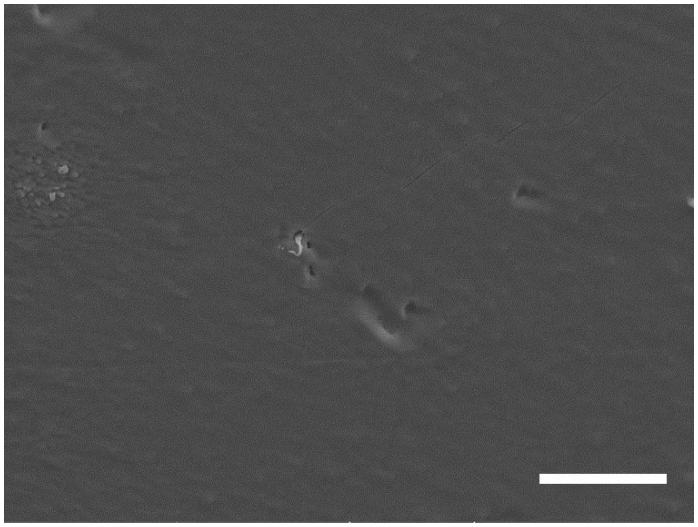

Figure S3. Top view of SEM images of $MAPbI_3$ SCs with spin-coating 2D HP layer, the scale bar is 50 μm.

Calculation of complex dielectric function.

Inspired by the literature reported before,[42] fitting the infrared spectrum based on the Gervais model, the high/low frequency dielectric constant ($\varepsilon_{\infty}/\varepsilon_{static}$), the lattice vibration transverse/longitudinal optical branch frequency (ω_{TO}/ω_{LO}) and the vibration attenuation factor (γ) are extracted. The complex dielectric function of $MAPbI_3$ is calculated by the following formula, where the subscript n represents the internal anisotropy of the material:

$$\varepsilon(\omega) = \varepsilon_{\infty} \prod_{n} \frac{\omega^2_{LO,n} - \omega^2 + i\gamma_{LO,n}\omega}{\omega^2_{TO,n} - \omega^2 + i\gamma_{TO,n}\omega} \tag{3}$$

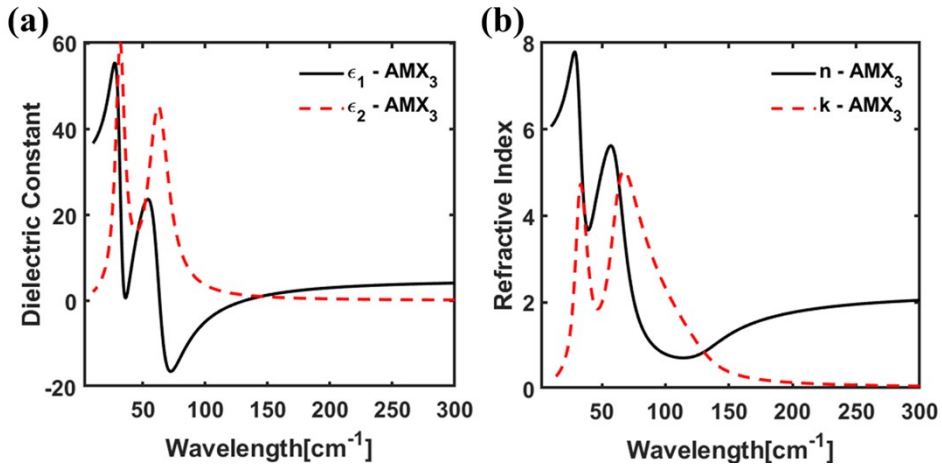

Figure S4. Recalculated a) complex permittivity ($\varepsilon_1+\varepsilon_2$i) and b) complex refractive index (n+ki) in far IR spectra of 30-300 cm^{-1}, according to the literature.[42]

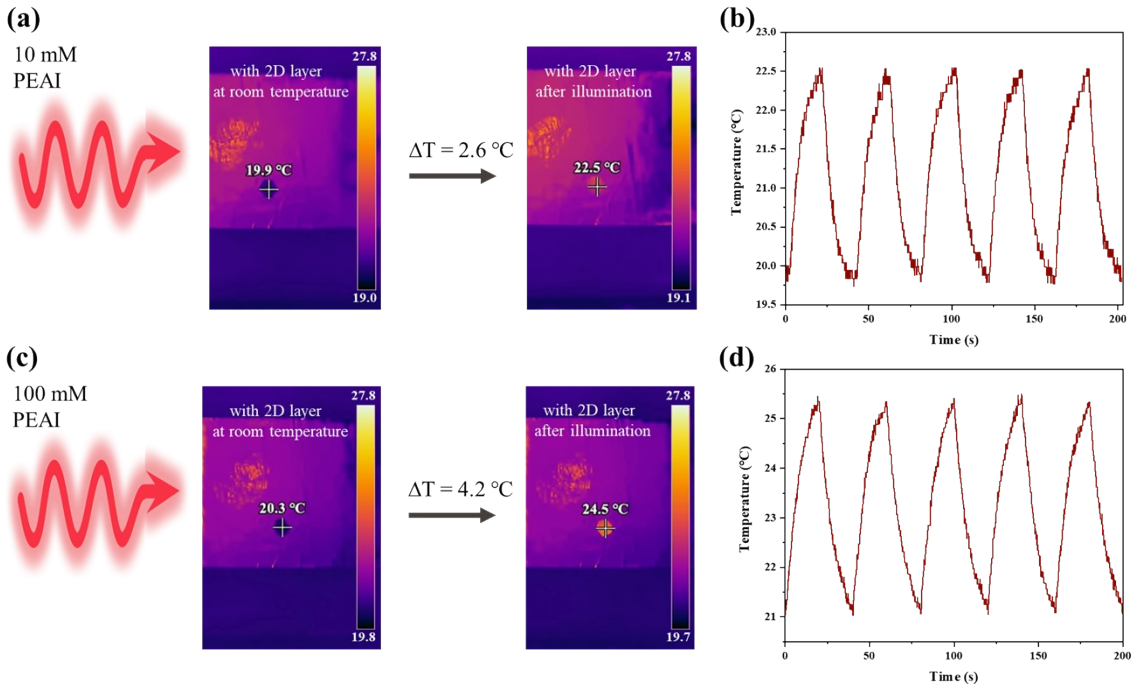

Figure S5. Infrared pictures and temperature-time curves of $MAPbI_3$ SCs spin-coated with different concentration of PEAI at 4000 rpm under THz irradiation cycle. a-b) 10 mM PEAI; c-d) 100 mM PEAI.

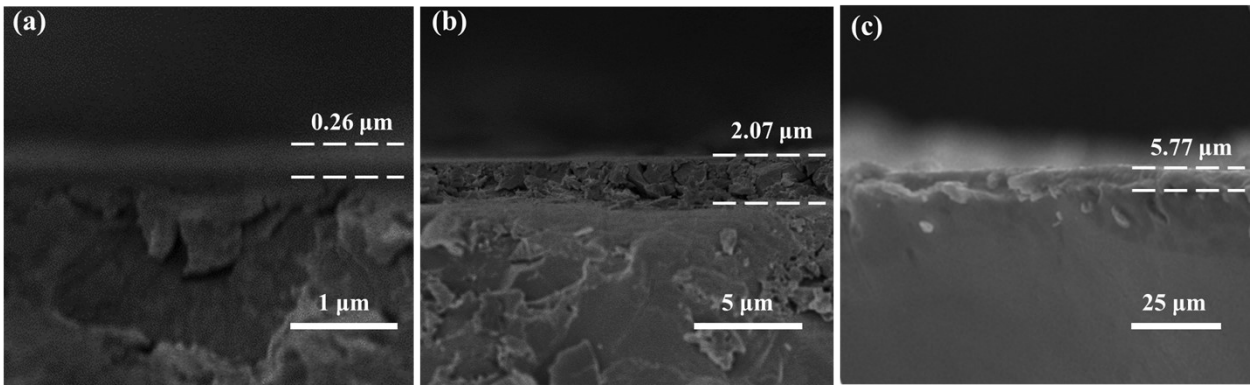

Figure S6. Thicknesses of 2D HP layers in $MAPbI_3$ SCs spin-coated with different concentration of PEAI. a) 10 mM PEAI; b) 100 mM PEAI; c) 500 mM PEAI.

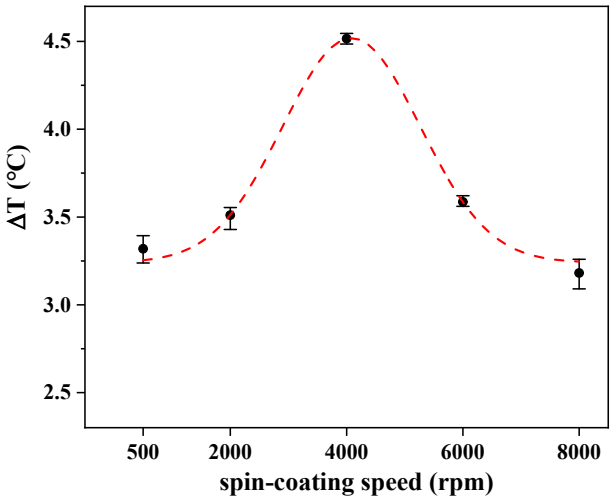

Figure S7. Temperature rise of $MAPbI_3$ SCs spin-coated with different spin-coating speed.

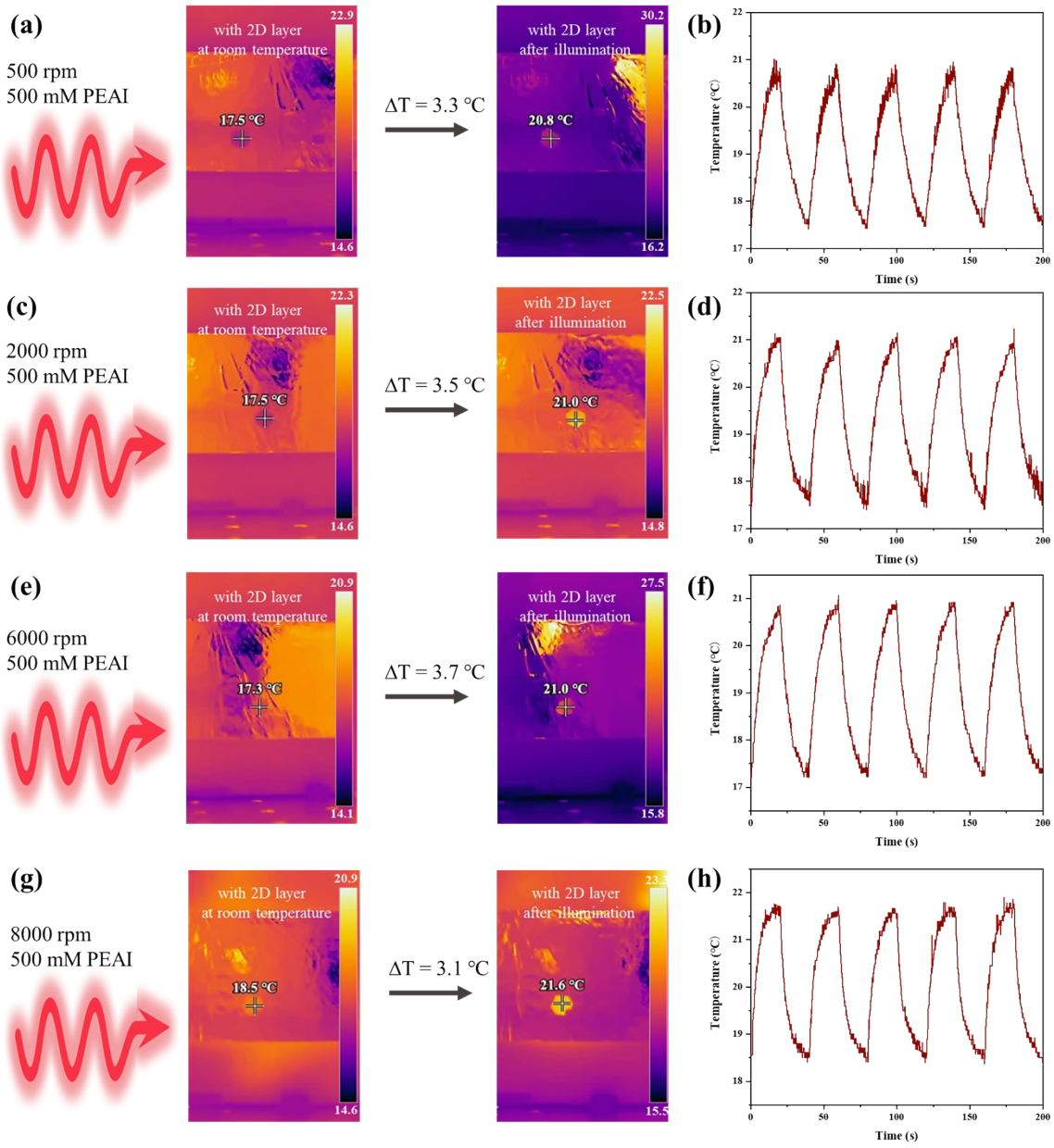

Figure S8. Infrared pictures and temperature-time curves of $MAPbI_3$ SCs spin-coated with 500 mM PEAI under THz irradiation cycle with different spin-coating speed. a-b) 500 rpm; c-d) 2000 rpm; e-f) 6000 rpm; g-h) 8000 rpm.

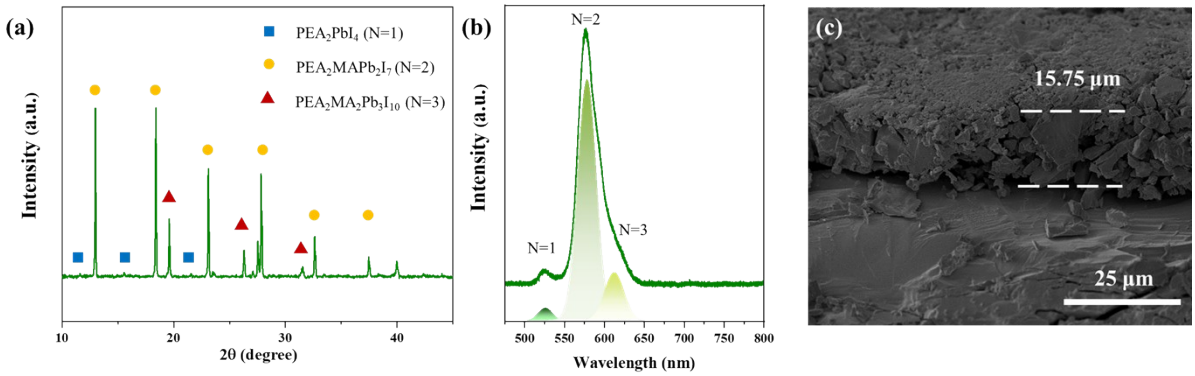

Figure S9. a) XRD pattern, b) PL plot, c) Cross-section view of SEM image of $MAPbI_3$ SC spin-coated with 500 mM PEAI at 500 rpm; of $MAPbI_3$ SC spin-coated with 500 mM PEAI at 500 rpm

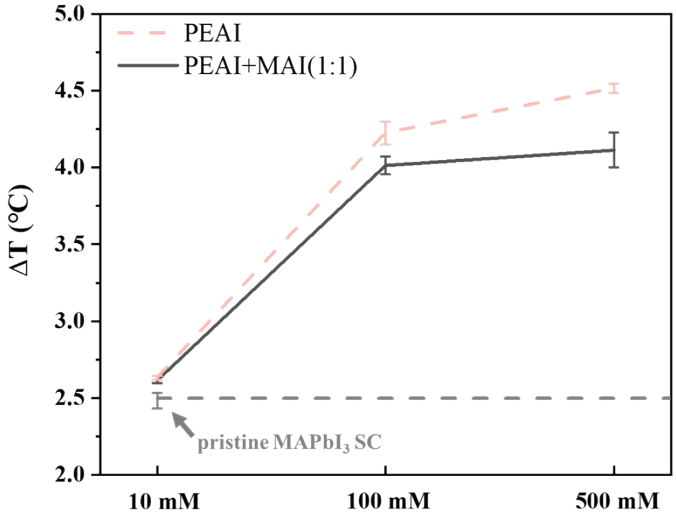

Figure S10. Temperature rise of $MAPbI_3$ SCs spin-coated with additive of MAI.

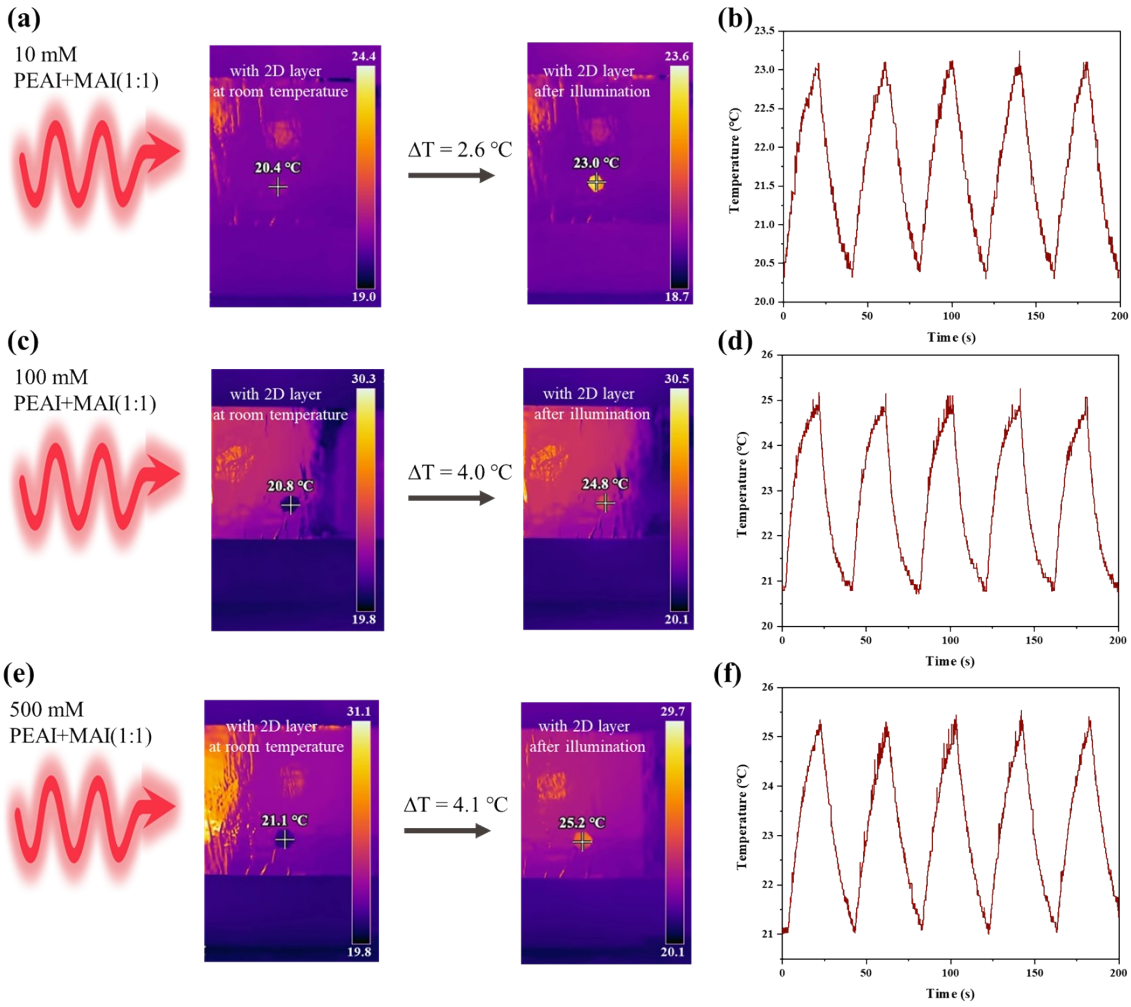

Figure S11. Infrared pictures and temperature-time curves of $MAPbI_3$ SCs spin-coated with additive of MAI under THz irradiation cycle. a-b) 10 mM; c-d) 100 mM; e-f) 500 mM.

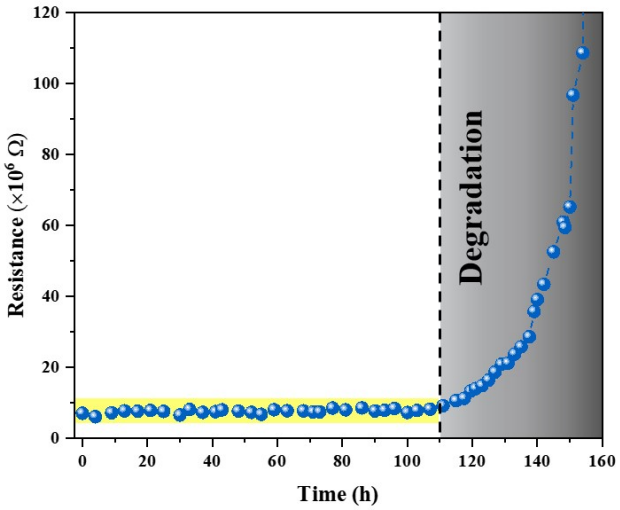

Figure S12. The stability of $MAPbI_3$ single crystal with Ag electrodes.

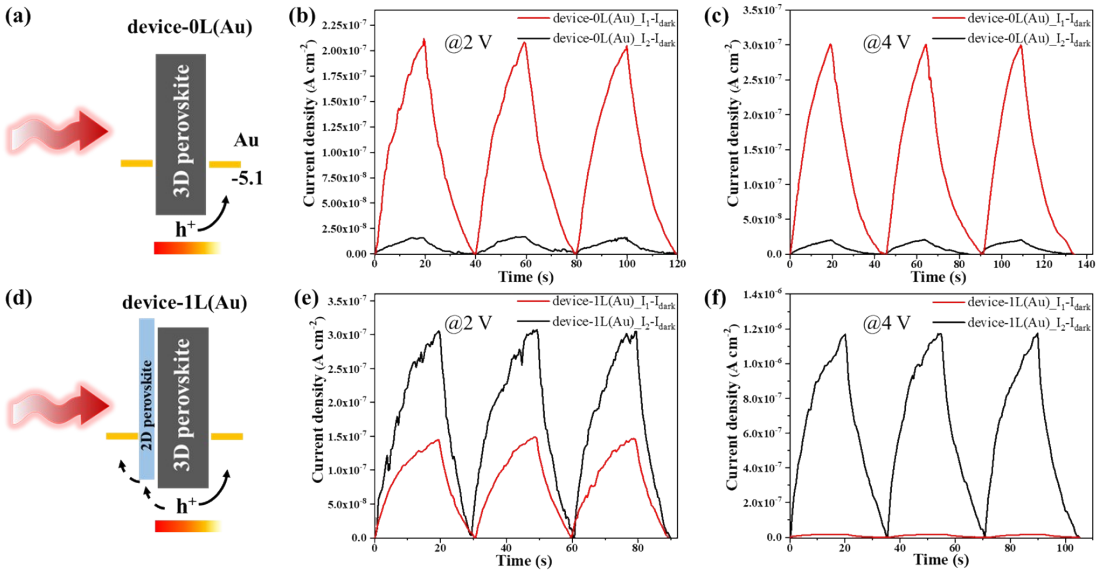

Figure S13. a) Energy band diagram of device-0(Au). *J-t* curves of device-0(Au) under different directions b) at 2 V and c) at 4 V. d) Energy band diagram of device-1(Au). *J-t* curves of device-1(Au) under different directions e) at 2 V and f) at 4 V.

It is reported that the majority carriers of HP SCs can be simply changed from holes to electrons by replacing the gold electrode with a silver electrode.[43, 44] Because the SCs

are usually in direct contact with the electrodes, Au can combine with organic molecules (MA^+) to form cation vacancies, while Ag reacts with halide ions to form anion vacancies.

Consistent with the literature,[43] device-0L(Au) presents good P-type (I_1-I_{dark}>I_2-I_{dark}, which means that the carriers moving from the hot end to the cold are holes), while for device-0L(Ag), it is the opposite N-type performance (I_1-I_{dark}<I_2-I_{dark}, the majority carriers are electrons). However, largely due to the heterojunction's attraction for holes, for device-1L(Au), I_1-I_{dark} dramatically decreases and becomes less than I_2-I_{dark} (contrary to device-0L(Au)), indicating that there is a driving force (heterojunction) hindering the movement of carriers from the hot end to the cold. Accordingly, the 2D layer is unfavorable for devices with Au electrodes, and thus the magnitude of each current cannot be accurately measured.

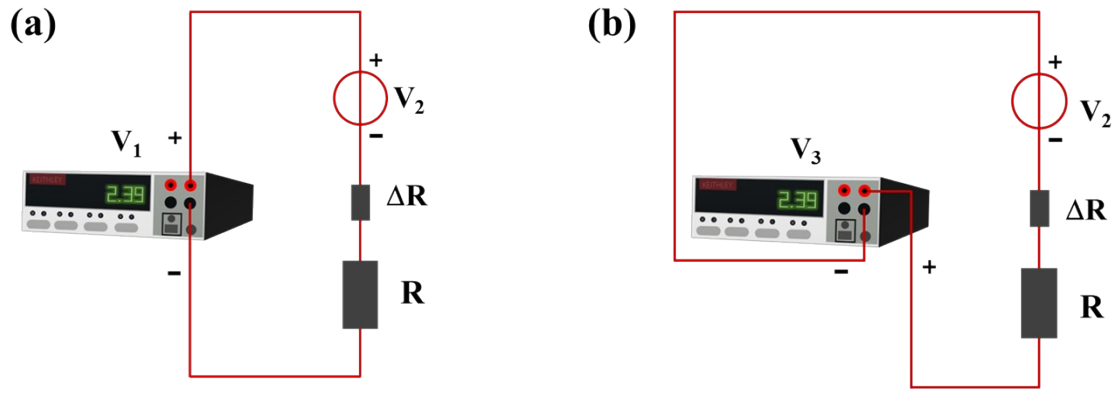

Figure S14. Equivalent circuit of 2D/3D HP SCs under THz irradiation. a) Applied voltage is opposite to V_{PTE}. b) Applied voltage is in the same direction as V_{PTE}.

The applied voltage V_1 and V_3 have the same value but in opposite directions.

Considering that the voltage generated by the PTE (Seebeck) effect can be equivalent to an additional voltage source ($V_{PTE} = S\Delta T$), when other parameters are fixed, the voltage generated by the PTE effect is the same, which is expressed as V_2.

Without THz illumination, V_2 generated by PTE effect and ΔR caused by bolometric are both zero, so the dark current $I_{dark1} = \frac{V_1}{R}$ (4) and $I_{dark2} = \frac{V_3}{R}$ (5).

With THz illumination, the currents I_1 and I_2 can be expressed as following:

$$\begin{aligned} I_1 &= \frac{V_1}{R+\Delta R} - \frac{V_2}{R+\Delta R} \\ &= \frac{V_1}{R} - \frac{V_1}{R} + \frac{V_1}{R+\Delta R} - \frac{V_2}{R+\Delta R} \\ &= \frac{V_1}{R} - \frac{V_1 \Delta R}{(R+\Delta R)R} - \frac{V_2}{R+\Delta R} \end{aligned} \tag{6}$$

$$\begin{aligned} I_2 &= \frac{V_3}{R+\Delta R} + \frac{V_2}{R+\Delta R} \\ &= \frac{V_3}{R} - \frac{V_3}{R} + \frac{V_3}{R+\Delta R} + \frac{V_2}{R+\Delta R} \\ &= \frac{V_3}{R} - \frac{V_3 \Delta R}{(R+\Delta R)R} + \frac{V_2}{R+\Delta R} \end{aligned} \tag{7}$$

$\frac{V_1}{R}$ ($\frac{V_3}{R}$) is the dark current, $-\frac{V_1 \Delta R}{(R+\Delta R)R}$ ($-\frac{V_3 \Delta R}{(R+\Delta R)R}$) is the result of current changes (ΔI) in the circuit due to resistance changes (ΔR). It is worth mentioning that since the resistance of perovskite materials decreases with increasing temperature, here $\Delta R<0$. And $\frac{V_2}{R+\Delta R}$ is simply the current generated by the additional voltage source due to the PTE effect. Thus, the measured current can be simplified to $I_1=I_{dark}+I_b-I_{PTE}$, and $I_2=I_{dark}+I_b+I_{PTE}$. Accordingly, the currents of different parts can be expressed as:

$$\Delta I_b = \frac{(I_1 - I_{dark1}) + (I_2 - I_{dark2})}{2} = -\frac{V_1 \Delta R}{(R+\Delta R)R} \tag{8}$$

$$I_{PTE} = \frac{(I_2 - I_{dark1}) - (I_1 - I_{dark2})}{2} = \frac{V_2}{R+\Delta R} \tag{9}$$

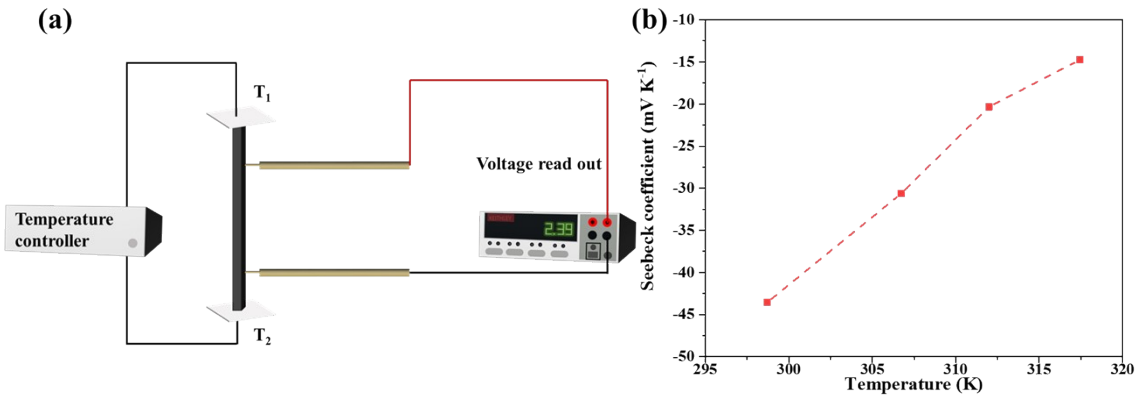

Figure S15. a) Schematic illustration of the Seebeck coefficient measurement. b) Seebeck coefficient of $MAPbI_3$(Ag) around room temperature.

The negative coefficient in Figure S15b indicates that the N-type nature of the SC with Ag electrodes.

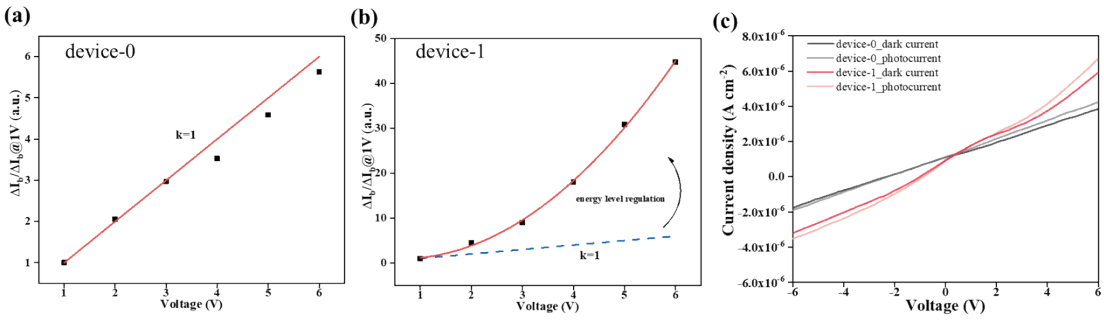

Figure S16. The ratio of ΔI_b at different voltages to 1V of a) device-0 and b) device-1. c) Dark and photo *J-V* curves of device-0 and device-1.

The relative current magnitude of Figure S16 is obtained from Fig. 4d. According to the above formulas, for ΔI_b, the derived equation is $\Delta I_b = -\frac{V_1 \Delta R}{(R+\Delta R)R}$. In Figure S16, the ratio of ΔI_b at different voltages to 1 V of device-0 exhibits good linear relationship, consistent with the ratio of $\frac{\Delta I_{b1}}{\Delta I_{b2}} = \frac{V_1}{V_2}$, proving the correctness of the theory. Due to the additional energy barriers, device-1 shows a deviation from the linear relationship. It shows that the heterojunction has a modulating effect on the electrical signal, and it becomes larger as the voltage increases.

References

1. T. Fang, J. Xin, C. Fu, D. Li, X. Zhao, C. Felser and T. Zhu, *Ann. Phys.*, 2020, **532**, 1900435.
2. L. Yang, N. Yang and B. Li, *Int. J. Heat Mass Transfer*, 2016, **99**, 102-106.
3. C. J. Glassbrenner and G. A. Slack, *Phys. Rev.*, 1964, **134**, 1058-1069.
4. G. Goncalves Dalkiranis, P. Ferrando-Villalba, A. Lopeandia-Fernandez, L. Abad-Munoz and J. Rodriguez-Viejo, *Sensors*, 2019, **19**, 1427.
5. S. Fust, A. Faustmann, D. J. Carrad, J. Bissinger, B. Loitsch, M. Doblinger, J. Becker, G. Abstreiter, J. J. Finley and G. Koblmuller, *Adv. Mater.*, 2020, **32**, 1905458.
6. X. Zou, X. Chen, H. Huang, Y. Xu and W. Duan, *Nanoscale*, 2015, **7**, 8776-8781.
7. C. Cai, L. Wei, X. Wu and D. Wang, *Microsyst. Technol.*, 2020, **27**, 243-249.
8. M. G. Holland, *Phys. Rev.*, 1964, **134**, 471-480.
9. S. D. Sharma, B. Khasimsaheb, Y. Y. Chen and S. Neeleshwar, *Ceram. Int.*, 2019, **45**, 2060-2068.
10. M.-L. Liu, F.-Q. Huang, L.-D. Chen and I. W. Chen, *Appl. Phys. Lett.*, 2009, **94**, 202103.
11. H. Yang, L. A. Jauregui, G. Zhang, Y. P. Chen and Y. Wu, *Nano Lett.*, 2012, **12**, 540-545.
12. H. Ju and J. Kim, *Chem. Eng. J.*, 2020, **402**, 126274.
13. R. Al Rahal Al Orabi, J. Hwang, C.-C. Lin, R. Gautier, B. Fontaine, W. Kim, J.-S. Rhyee, D. Wee and M. Fornari, *Chem. Mater.*, 2016, **29**, 612-620.
14. S.-X. Lin, X. Tan, H. Shao, J. Xu, Q. Wu, G.-Q. Liu, W.-H. Zhang and J. Jiang, *J. Phys. Chem. C*, 2019, **123**, 15996-16002.

15. Y.-X. Chen, Z.-H. Ge, M. Yin, D. Feng, X.-Q. Huang, W. Zhao and J. He, *Adv. Funct. Mater.*, 2016, **26**, 6836-6845.
16. M. R. Burton, T. Liu, J. McGettrick, S. Mehraban, J. Baker, A. Pockett, T. Watson, O. Fenwick and M. J. Carnie, *Adv. Mater.*, 2018, **30**, 1801357.
17. J. Li, X. Zhang, Z. Chen, S. Lin, W. Li, J. Shen, I. T. Witting, A. Faghaninia, Y. Chen, A. Jain, L. Chen, G. J. Snyder and Y. Pei, *Joule*, 2018, **2**, 976-987.
18. W. D. Liu, D. Z. Wang, Q. Liu, W. Zhou, Z. Shao and Z. G. Chen, *Adv. Energy Mater.*, 2020, **10**, 2000367.
19. L. Yang, J. Q. Li, R. Chen, Y. Li, F. S. Liu and W. Q. Ao, *J. Electron. Mater.*, 2016, **45**, 5533-5539.
20. J. P. Heremans, V. Jovovic, E. S. Toberer, A. Saramat, K. Kurosaki, A. Charoenphakdee, S. Yamanaka and G. J. Snyder, *Science*, 2008, **321**, 554-557.
21. K. F. Hsu, S. Loo, F. Guo, W. Chen, J. S. Dyck, C. Uher, T. Hogan, E. K. Polychroniadis and M. G. Kanatzidis, *Science*, 2004, **303**, 818-821.
22. L. D. Zhao, S. H. Lo, J. He, H. Li, K. Biswas, J. Androulakis, C. I. Wu, T. P. Hogan, D. Y. Chung, V. P. Dravid and M. G. Kanatzidis, *J. Am. Chem. Soc.,* 2011, **133**, 20476-20487.
23. Y.-L. Pei, J. He, J.-F. Li, F. Li, Q. Liu, W. Pan, C. Barreteau, D. Berardan, N. Dragoe and L.-D. Zhao, *NPG Asia Mater.*, 2013, **5**, e47.
24. X. Zhang, C. Chang, Y. Zhou and L. D. Zhao, *Materials*, 2017, **10**, 198.
25. Z. Zhou, X. Tan, G. Ren, Y. Lin and C. Nan, *J. Electron. Mater.*, 2016, **46**, 2593-2598.
26. X. Tang, B. Zhang, X. Zhang, S. Wang, X. Lu, G. Han, G. Wang and X. Zhou, *ACS Appl. Mater. Interfaces*, 2020, **12**, 8359-8365.
27. J. Zhang, L. Song and B. B. Iversen, *Adv. Sci.*, 2020, **7**, 2002867.
28. Y. Zheng, C. Liu, L. Miao, C. Li, R. Huang, J. Gao, X. Wang, J. Chen, Y. Zhou and E. Nishibori, *Nano Energy*, 2019, **59**, 311-320.
29. P. Ying, X. Li, Y. Wang, J. Yang, C. Fu, W. Zhang, X. Zhao and T. Zhu, *Adv. Funct. Mater.*, 2017, **27**, 1604145.
30. Z. Liu, Y. Wang, J. Mao, H. Geng, J. Shuai, Y. Wang, R. He, W. Cai, J. Sui and Z. Ren, *Adv. Energy Mater.*, 2016, **6**, 1502269.
31. L.-D. Zhao, B.-P. Zhang, W.-S. Liu and J.-F. Li, *J. Appl. Phys.*, 2009, **105**, 023704.
32. L.-D. Zhao, B.-P. Zhang, J.-F. Li, M. Zhou, W.-S. Liu and J. Liu, *J. Alloys Compd.*, 2008, **455**, 259-264.
33. B. Poudel, Q. Hao, Y. Ma, Y. Lan, A. Minnich, B. Yu, X. Yan, D. Wang, A. Muto, D. Vashaee, X. Chen, J. Liu, M. S. Dresselhaus, G. Chen and Z. Ren, *Science*, 2008, **320**, 634-638.
34. C.-C. Lin, D. Ginting, G. Kim, K. Ahn and J.-S. Rhyee, *Curr. Appl. Phys.*, 2018, **18**, 1534-1539.
35. Y. Zhu, J. Carrete, Q.-L. Meng, Z. Huang, N. Mingo, P. Jiang and X. Bao, *J. Mater. Chem. A*, 2018, **6**, 7959-7966.
36. P. C. Wei, S. Bhattacharya, J. He, S. Neeleshwar, R. Podila, Y. Y. Chen and A. M. Rao, *Nature*, 2016, **539**, E1-E2.
37. G. A. Elbaz, W. L. Ong, E. A. Doud, P. Kim, D. W. Paley, X. Roy and J. A. Malen,

Nano Lett., 2017, **17**, 5734-5739.
38. M. A. Haque, S. Kee, D. R. Villalva, W. L. Ong and D. Baran, *Adv. Sci.*, 2020, **7**, 1903389.
39. T. Haeger, R. Heiderhoff and T. Riedl, *J. Mater. Chem. C*, 2020, **8**, 14289-14311.
40. M. Samiee, S. Konduri, B. Ganapathy, R. Kottokkaran, H. A. Abbas, A. Kitahara, P. Joshi, L. Zhang, M. Noack and V. Dalal, *Appl. Phys. Lett.*, 2014, **105**, 153502.
41. F. Brivio, A. B. Walker and A. Walsh, *APL Mater.*, 2013, **1**, 042111.
42. M. Sendner, P. K. Nayak, D. A. Egger, S. Beck, C. Müller, B. Epding, W. Kowalsky, L. Kronik, H. J. Snaith, A. Pucci and R. Lovrinčić, *Mater. Horiz*, 2016, **3**, 613-620.
43. Z. Xie, K. Feng, Y. Xiong, X. Chen, Y. Liang, K. Abid and L. Xu, *Adv. Electron. Mater.*, 2021, **7**, 2001003.
44. T. Wu, R. Mukherjee, O. S. Ovchinnikova, L. Collins, M. Ahmadi, W. Lu, N. G. Kang, J. W. Mays, S. Jesse, D. Mandrus and B. Hu, *J. Am. Chem. Soc.*, 2017, **139**, 17285-17288.